Eigenspectrum, Chern numbers and phase diagrams of ultracold color-orbit-coupled SU(3) fermions in optical lattices

Man Hon Yau and C. A. R. Sá de Melo
School of Physics, Georgia Institute of Technology, Atlanta, Georgia 30332, USA

(Received 13 November 2020; revised 9 March 2021; accepted 12 March 2021; published 1 April 2021)

We study ultracold color fermions with three internal states, red, green, and blue, with SU(3) symmetry in optical lattices, when color-orbit coupling and color-flip fields are present. This system corresponds to a generalization of two internal state fermions with SU(2) symmetry in the presence of spin-orbit coupling and spin-flipping Zeeman fields. We investigate the eigenspectrum and Chern numbers to describe different topological phases that emerge in the phase diagrams of color-orbit coupled fermions in optical lattices. We obtain the phases as a function of artificial magnetic, color-orbit, and color-flip fields that can be independently controlled. For fixed artificial magnetic flux ratio, we identify topological quantum phases and phase transitions in the phase diagrams of chemical potential versus color-flip fields or color-orbit coupling, where the chirality and number of midgap edge states changes. The topologically nontrivial phases are classified in three groups: The first group has total nonzero chirality and exhibits only the quantum charge Hall effect; the second group has total nonzero chirality and exhibits both quantum charge and quantum color Hall effects; and the third group has total zero chirality but exhibits the quantum color Hall effect. These phases are generalizations of the quantum Hall and quantum spin Hall phases for charged spin-1/2 fermions. Lastly, we also describe the color density of states and a staircase structure in the total and color filling factors versus chemical potential for fixed color-orbit coupling, color-flip field, and magnetic flux ratio. We show the existence of incompressible states at rational filling factors precisely given by a gap labelling theorem that relates the filling factors to the magnetic flux ratio and topological quantum numbers.

DOI: 10.1103/PhysRevA.103.043302

I. INTRODUCTION

Ultracold fermions loaded in optical lattices have become ideal systems to study related electronic phase diagrams and transport properties, because they provide a clean and well-controlled playground to change various lattice parameters and external fields at the turn of a knob. While several experimental groups have worked mostly with Fermi isotopes ^{6}Li and ^{40}K using two internal states to study various aspects of interacting SU(2) fermions, there has been a growing interest in studying SU(N) generalizations of these systems. Examples of atomic SU(N) fermions found in nature are fermionic isotopes of closed-shell atoms with two electrons in their outer electronic configuration. Two systems have been studied by several groups: One of them is ^{173}Yb, a fermionic isotope of ytterbium, and the other is ^{87}Sr, a fermionic isotope of strontium.

The fermionic isotope ^{173}Yb has electronic shell structure $[\mathrm{Xe}]4f^{14}6s^2$, with electronic spin $S = 0$ and nuclear spin $I = 5/2$. The electronic ground state of ^{173}Yb is $^1S_0$, which is sixfold degenerate because of its nuclear spin. The six degenerate states have nuclear spin projections $m_{\mathrm{I}} = \{\pm 5/2, \pm 3/2, \pm 1/2\}$. Atoms in any selected state can be manipulated out of a trap or transformed into a desired nuclear spin state, so that the ground state of trapped ^{173}Yb can be up to sixfold degenerate [1–6].

The fermionic isotope ^{87}Sr has electronic shell structure $[\mathrm{Kr}]5s^2$, with electronic spin $S = 0$ and nuclear spin $I = 9/2$. The electronic ground state of ^{87}Sr is $^1S_0$, which is tenfold degenerate because of its nuclear spin. The ten degenerate states have nuclear spin projection $m_{\mathrm{I}} = \{\pm 9/2, \pm 7/2, \pm 5/2, \pm 3/2, \pm 1/2\}$. Again, atoms in any selected state can be manipulated out of a trap or transformed into a desired nuclear spin state, so that the ground state of trapped ^{87}Sr can be up to tenfold degenerate [7–10]. In addition, interactions between these closed-shell atoms are independent of their nuclear spin states at the atomic energy scales of interest, and therefore interactions are SU(N) symmetric. Since experiments are conducted at very low temperatures, the collisional properties of these atoms are dominated by s-wave scattering, and the interactions are local in space; that is, they are contact interactions described by a delta function potential that is independent of the nuclear spin states of the atoms. As a result, ^{173}Yb can be up to SU(6) symmetric while ^{87}Sr can be up to SU(10) symmetric in their nuclear spin projections. In addition, orbital Feshbach resonances can be used to control the strength of the SU(N)-symmetric interactions from weak to strong [11,12]. Since any three nuclear states of ^{173}Yb or ^{87}Sr can be selected and trapped in an optical lattice, we label these nuclear states by color $\{R, G, B\}$ or pseudospin $\{\uparrow, 0, \downarrow\}$ to describe a Fermi system with SU(3) symmetry.

The creation of artificial gauge fields in the context of ultracold atoms has been discussed in recent reviews [13,14]. It is now possible to create artificial magnetic fields [15] in

optical lattices [16,17] that mimic electronic materials exhibiting integer [18] and fractional [19] quantum Hall effects. The synthetic magnetic flux values created in optical lattices [16,17] are sufficiently large to allow for the experimental exploration of the intricacies of Harper's model [20] and the Hofstadter butterfly [21], as well as the experimental determination of Chern numbers [22]. In addition, artificial magnetic fields for SU(2) fermions in optical lattices could be used to simulate the phenomenon of magnetic field induced reentrant superfluidity, as discussed in the context of superconductivity in condensed matter physics for spin-1/2 fermions in standard lattices [23–26]. Furthermore, the creation of artificial spin-orbit coupling for ultracold atoms [27] also allows for the simulation of electronic materials exhibiting the quantum spin Hall effect [28–30].

For ultracold fermions in optical lattices, artificial magnetic fields enable studies of topological insulators that break time-reversal symmetry, such as quantum Hall systems, while artificial spin-orbit fields allow for studies of topological insulators that do not break time-reversal symmetry, such as quantum spin Hall systems. Both types of topological insulators are characterized by Berry curvatures and Chern numbers, which have been measured experimentally using time-of-flight techniques [31], inspired by theoretical proposals [32,33], and using dynamics of the center of mass of the atomic cloud [34], also motivated by theoretical work [35,36]. However, studies of ultracold fermions may go beyond the quantum simulation of spin-1/2 topological insulators under typical condensed matter conditions [37], because artificial magnetic, spin-orbit, and Zeeman fields may be adjusted independently [38].

Artificial magnetic, spin-orbit, and Zeeman fields in spin-1/2 ultracold Fermi atoms may be independently tuned via a combination of experimental techniques that produce artificial magnetic fluxes without using internal states, such as laser-assisted tunneling [16,17], and that produce spin-orbit and Zeeman fields using internal states, such as Raman processes [27] or radio-frequency atom chips [39,40]. These techniques can also be applied to SU(3) fermions with three internal states (colors) and allow for the investigation of exotic topological insulating phases that arise in optical lattices when artificial magnetic, color-orbit, and color-flip fields are varied. The present system in optical lattices expands the realm of phases beyond Fermi liquid and superfluid for SU(3) fermions in the presence of color-orbit and color-flip fields analyzed in the continuum or in harmonic traps [41,42].

In this paper, we study the interplay of artificial magnetic, color-orbit, and color-flip fields for ultracold SU(3) fermions with three internal states (colors) and their effects on topological insulators in regimes that cannot be reached or found in condensed matter physics. We investigate the eigenspectrum and Chern numbers to describe different topological phases that emerge in the phase diagrams of color-orbit-coupled fermions in optical lattices. We obtain the phases as a function of artificial magnetic, color-orbit, and color-flip fields that can be independently controlled. For a fixed artificial magnetic flux ratio, we identify the topological quantum phases and phase transitions in the phase diagrams of chemical potential versus color-flip fields or color-orbit coupling, where the chirality and number of midgap edge states change. The topologically nontrivial phases are classified in three groups: The first group has total nonzero chirality and exhibits only the quantum charge Hall effect, the second group has total nonzero chirality and exhibits both quantum charge and quantum color Hall effects, and the third group has total zero chirality but exhibits the quantum color Hall effect. These phases are generalizations of the quantum Hall and quantum spin Hall phases for charged spin-1/2 fermions. Lastly, we also describe the color density of states and a staircase structure in the total and color filling factors versus chemical potential for fixed color-orbit coupling, color-flip field, and magnetic flux ratio. We show the existence of incompressible states at rational filling factors precisely given by a gap labeling theorem that relates the filling factors to the magnetic flux ratio and topological numbers.

The remainder of this paper is organized as follows. In Sec. II, we describe the three-color Hamiltonian for ultracold fermions loaded into a square optical lattice and in the presence of artificial magnetic, color-orbit, and color-flip fields. In Sec. III, we analyze the energy spectrum obtained from a generalized Harper's matrix with open boundary conditions and obtain the energy dispersions for bulk and edge states. In Sec. IV, we discuss the color Chern numbers to classify the insulating phases in the *charge* sector. We compute the Chern numbers via the Berry curvatures associated with the eigenstates of the Hamiltonian with periodic boundary conditions. We confirm the existence of a bulk-edge correspondence by comparing the Chern number calculated via periodic boundary conditions to the number of chiral edge states obtained via open boundary conditions. In Sec. V, we discuss the gap labeling theorem and give a physical interpretation to the topological quantum numbers. In Sec. VI, we describe the phase diagrams of chemical potential versus color-flip field (Sec. VI A) and the phase diagrams of chemical potential versus color-orbit coupling (Sec. VI B). We identify phases that exhibit quantum charge Hall and quantum color Hall effects in analogy to the quantum Hall effect and quantum spin Hall effect for spin-1/2 systems, and we find phases that exhibit simultaneously quantum charge and color Hall effects, which do not exist in spin-1/2 systems. These phases are topological insulators. In Sec. VII, we analyze the color density of states for the system with periodic boundary conditions and show that the bulk gaps match precisely with the gaps obtained for open boundary conditions. Furthermore, we compute directly the filling factor as a function of the chemical potential and reveal the existence of filling factor steps at the precise values given by the gap labeling theorem discussed in Sec. V to describe insulating states. In Sec. VIII, we discuss the effects of weak interactions on topological insulating phases and their edge states. Finally, in Sec. IX, we summarize our results and state our conclusions.

II. THREE-COLOR HAMILTONIAN

To discuss the phase diagrams and Chern numbers of colored fermions with three internal states red (R), green (G), and blue (B) in optical lattices, we consider a lattice extension of the continuum color Hamiltonian with color-dependent momentum transfer k_T and color-flip fields h_x [41,42], which also includes a Peierls substituted [43] artificial vector potential

$(0, \mathcal{A}_y, 0)$. As described in Sec. I, the vector potential $\mathcal{A}_y$ may be generated by laser-assisted tunneling [16,17], while the color-dependent momentum transfer k_T and color-flip field h_x may be created via counterpropagating Raman beams [27] or via radio-frequency atom chips [39,40].

We assume that the fermions are trapped in a two-dimensional square optical lattice and are described by the Hamiltonian operator matrix of ultracold atoms with three internal states

$$\hat{\mathbf{H}} = \begin{pmatrix} \varepsilon_R(\hat{\mathbf{k}}) & -h_x/\sqrt{2} & 0 \\ -h_x/\sqrt{2} & \varepsilon_G(\hat{\mathbf{k}}) & -h_x/\sqrt{2} \\ 0 & -h_x/\sqrt{2} & \varepsilon_B(\hat{\mathbf{k}}) \end{pmatrix}, \tag{1}$$

when written in first quantization. In Eq. (1), the term

$$\varepsilon_R(\hat{\mathbf{k}}) = -2t\{\cos[(\hat{k}_x - k_T)a] + \cos[(\hat{k}_y - \mathcal{A}_y)a]\} \tag{2}$$

corresponds to the kinetic energy of the R state including the momentum transfer $+k_T$ along the x direction, arising from counterpropagating Raman beams [27] or radio-frequency atom chips [39,40], and the vector potential $\mathcal{A}_y$ along the y direction, arising from laser-assisted tunneling [16,17]. The term

$$\varepsilon_G(\hat{\mathbf{k}}) = -2t\{\cos(\hat{k}_x a) + \cos[(\hat{k}_y - \mathcal{A}_y)a]\} \tag{3}$$

corresponds to the kinetic energy of the G state, which experiences no momentum transfer but feels the presence of $\mathcal{A}_y$, and

$$\varepsilon_B(\hat{\mathbf{k}}) = -2t\{\cos[(\hat{k}_x + k_T)a] + \cos[(\hat{k}_y - \mathcal{A}_y)a]\} \tag{4}$$

corresponds to the kinetic energy of the B state, including the momentum transfer $-k_T$ along the x direction and the vector potential $\mathcal{A}_y$ along the y direction.

In Eqs. (2), (3), and (4), the parameter t is the hopping amplitude, a is the lattice spacing, k_T is the color-dependent momentum transfer along the x direction (artificial unidirectional color-orbit coupling), and $\mathcal{A}_y = eHx/\hbar c$ plays the role of the y component of the artificial vector potential, where H is identified as a synthetic magnetic field along the z axis. Notice that $\mathcal{A}_y$ has dimensions of inverse length. It is important to emphasize that the system is neutral, so there is no charge e, that is, $\mathcal{A}_y a$ should be just viewed as a position-dependent phase $\phi(x) = \mathcal{A}_y a$. Lastly, h_x represents a color-flip field along the x direction, whose physical origin is a Rabi term that couples the red and green as well as the green and blue internal states of the atom.

The Hamiltonian matrix in Eq. (1) acts on a three-color wave function $\mathbf{\Psi}(\mathbf{r}) = [\Psi_R(\mathbf{r}), \Psi_G(\mathbf{r}), \Psi_B(\mathbf{r})]^T$, where T indicates transposition and $\mathbf{r} = (x, y)$ labels the coordinates in the square lattice. An analogy to pseudospin-1 fermions or spin-1 bosons in optical lattices can be made by rewriting Eq. (1) in terms of spin-1 matrices $\mathbf{J}_\ell$, with $\ell = \{x, y, z\}$ as

$$\hat{\mathbf{H}} = \varepsilon_G(\hat{\mathbf{k}})\mathbf{1} - h_x\mathbf{J}_x - h_z(\hat{\mathbf{k}})\mathbf{J}_z + g_z(\hat{\mathbf{k}})\mathbf{J}_z^2, \tag{5}$$

where h_x plays the role of a Zeeman field along the x axis in spin space, $h_z(\hat{\mathbf{k}}) = [\varepsilon_B(\hat{\mathbf{k}}) - \varepsilon_R(\hat{\mathbf{k}})]/2$ represents momentum-dependent Zeeman field along the z axis in spin space, and $g_z(\hat{\mathbf{k}}) = [\varepsilon_B(\hat{\mathbf{k}}) + \varepsilon_R(\hat{\mathbf{k}})]/2 - \varepsilon_G(\hat{\mathbf{k}})$ describes a momentum-dependent quadratic Zeeman shift along the z axis in spin space, and thus can be viewed as a spin (color) quadrupolar effect. The color states $\{R, G, B\}$ are directly mapped into pseudospin-1 states $\{\uparrow, 0, \downarrow\}$. Notice that the presence of the color fields h_x, $h_z(\hat{\mathbf{k}})$, and $g_z(\hat{\mathbf{k}})$ breaks the SU(3) symmetry of otherwise degenerate color bands. To make some connections to quantum chromodynamics (QCD), we note that the independent-particle Hamiltonian described in Eqs. (1) or (5) in general does not commute with the Gell-Mann matrices $\boldsymbol{\lambda}_j$, which are the eight generators of SU(3). To visualize this clearly, it is sufficient to recall that the angular momentum matrices $\mathbf{J}_\ell$ can be written in terms of $\boldsymbol{\lambda}_j$ as $\mathbf{J}_x = (\boldsymbol{\lambda}_1 + \boldsymbol{\lambda}_6)/2$, $\mathbf{J}_y = (\boldsymbol{\lambda}_2 + \boldsymbol{\lambda}_7)/2$, and $\mathbf{J}_z = (\boldsymbol{\lambda}_3 + \sqrt{3}\boldsymbol{\lambda}_8)/2$ and to show that the commutator $[\hat{\mathbf{H}}, \boldsymbol{\lambda}_j] \neq 0$. The Hamiltonian in Eqs. (1) or (5) becomes SU(3) invariant only when the fields $h_x = h_z(\hat{\mathbf{k}}) = g_z(\hat{\mathbf{k}}) = 0$, rendering $\hat{\mathbf{H}}$ diagonal and proportional to the unit matrix $\mathbf{1}$; that is, all color states become degenerate.

The Hamiltonian given in Eq. (1) is formally the Fourier-transformed operator of a tight-binding real-space lattice Hamiltonian with N_x sites along the x direction and N_y sites along the y direction in the presence of a Peierls substituted [43] vector potential $\mathcal{A}_y$, and color-orbit momentum shifts $\pm k_T a$ along the x direction. The boundary conditions are not directly reflected on that operator but are explicitly required on its wave functions depending on geometrical constraints. Generally, there are three types of geometrical constraints that one can use. The first geometry is a two-dimensional sheet of dimensions $L_x = N_x a$ and $L_y = N_y a$ with open boundaries along the x and y directions. The second one is a cylindrical geometry, where periodic boundary conditions are imposed in one direction and open boundaries in the other. The third one is a toroidal geometry, where periodic boundary conditions are imposed in both directions.

It is important to emphasize that, under standard experimental conditions, two-dimensional optical lattices are created in the sheet geometry mentioned above. In this case, the system has open boundaries both along the x and y directions and can develop edge states in all four edges. However, throughout the paper, we will be using the other two types of boundary conditions, as they offer calculational advantages without compromising the physics that we would like to elucidate. When we are interested solely in bulk properties, we use a real-space toroidal geometry with periodic boundary conditions along the x and y directions. However, when we are curious about edge-state properties, we work with a cylindrical geometry having finite number of sites N_x along the x direction but periodic boundary conditions along the y direction.

Having described the Hamiltonian of our system in this section, we discuss next the eigenspectrum associated with the Hamiltonian matrix described in Eqs. (1) or (5).

III. HARPER'S EIGENSPECTRUM

In this section, we obtain the eigenspectrum of the Hamiltonian in Eqs. (1) or (5), for the cylindrical geometry, as we would like to analyze the emergence of edge states. Given that the gauge potential $\mathcal{A}_y$ depends only on x, the momentum k_y is a good quantum number while k_x is not. Thus, we impose periodic boundary conditions along the y direction and consider a finite lattice along the x direction with N_x sites. In this

case, we can transform the Hamiltonian from Eq. (1) into the color-dependent Harper's matrix

$$\mathbf{H} = \begin{pmatrix} \ddots & \mathbf{B} & \mathbf{0} & \mathbf{0} & \mathbf{0} \\ \mathbf{B}^* & \mathbf{A}_{m-1} & \mathbf{B} & \mathbf{0} & \mathbf{0} \\ \mathbf{0} & \mathbf{B}^* & \mathbf{A}_m & \mathbf{B} & \mathbf{0} \\ \mathbf{0} & \mathbf{0} & \mathbf{B}^* & \mathbf{A}_{m+1} & \mathbf{B} \\ \mathbf{0} & \mathbf{0} & \mathbf{0} & \mathbf{B}^* & \ddots \end{pmatrix}, \tag{6}$$

which has a tridiagonal block structure that couples neighboring sites $(m-1, m, m+1)$ along the x direction and possesses discrete translational invariance along the y axis. This is a generalization of the Harper's matrix for spin-1/2 fermions with two internal states [20]. The matrices $\mathbf{A}$ and $\mathbf{B}$ and the null matrix $\mathbf{0}$ consist of 3×3 blocks with entries labeled by internal color states $\{R, G, B\}$ or pseudospin-1 states $\{\uparrow, 0, \downarrow\}$. The size of the space labeled by the site index m is N_x, and thus the total dimension of the matrix $\mathbf{H}$ in Eq. (6) is $3N_x \times 3N_x$. The matrix indexed by position $x = ma$ is

$$\mathbf{A}_m = \begin{pmatrix} \mathbf{A}_{mR} & -h_x/\sqrt{2} & 0 \\ -h_x/\sqrt{2} & \mathbf{A}_{mG} & -h_x/\sqrt{2} \\ 0 & -h_x/\sqrt{2} & \mathbf{A}_{mB} \end{pmatrix},$$

with $\mathbf{A}_{mR} = \mathbf{A}_{mG} = \mathbf{A}_{mB} = -2t\cos(k_y a - 2\pi m\alpha)$, where the parameter $\alpha = \Phi/\Phi_0$ represents the ratio between the magnetic flux through a lattice plaquette $\Phi = Ha^2$ and the flux quantum $\Phi_0 = hc/e$, or the ratio between the plaquette area a^2 and the square of the magnetic length $\ell_M = \sqrt{hc/eH}$, that is, $\alpha = (a/\ell_M)^2$. The matrix that contains the color-orbit coupling is

$$\mathbf{B} = \begin{pmatrix} -te^{-ik_T a} & 0 & 0 \\ 0 & -t & 0 \\ 0 & 0 & -te^{ik_T a} \end{pmatrix},$$

where k_T $(-k_T)$ corresponds to the momentum transfer along the x direction for state R (B), while the momentum transfer for state G is zero.

The full Hofstadter spectrum [21] of energy E versus flux ratio $\alpha = \Phi/\Phi_0$ for colored fermions can be obtained from the eigenvalues of the Harper's matrix defined in Eq. (6). However, in this work, we focus on a fixed value of α and discuss the energy spectrum as a function of the color-orbit coupling k_T and color-flip field h_x. We consider $N_x = 50$ sites along the x direction, with three states $\{R, G, B\}$ per site, but periodic boundary conditions along the y direction. The eigenvalues $E_{n_\beta}(k_y)$ are labeled by a discrete band index n_β and by momentum k_y and are functions of the color-orbit coupling k_T, color-flip field h_x, and flux ratio $\alpha = \Phi/\Phi_0$. The index β in n_β is a reminder that the resulting bands carry a mixed-color index β; when color is conserved, the index β labels $\{R, G, B\}$ states.

In Fig. 1, we show $E_{n_\beta}(k_y)$ for flux ratio $\alpha = 1/3$ in the cases (a) $k_T a = 0$ and $h_x/t = 0$, where there are three sets of color-degenerate bulk bands connected by color-degenerate midgap edge bands (there are three sets because the magnetic flux ratio is $\alpha = 1/3$); (b) $k_T a = \pi/8$ and $h_x/t = 0$, which is identical to case (a) because of a color-gauge symmetry that allows gauging away the color-orbit coupling; (c) $k_T a = 0$ and $h_x/t = 2.0$, where there are nine sets of bulk bands with

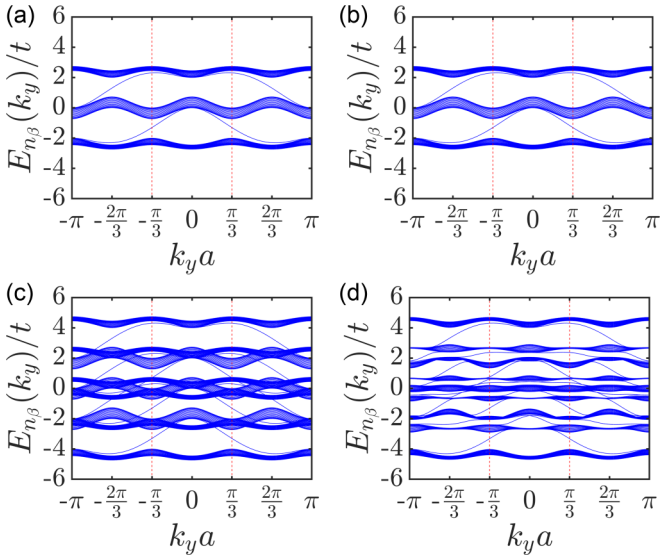

FIG. 1. Eigenvalues $E_{n_\beta}(k_y)/t$ of the color-dependent Harper's matrix vs $k_y a$ for magnetic flux ratio $\alpha = 1/3$. The parameters are (a) $k_T a = 0$ and $h_x/t = 0$, (b) $k_T a = \pi/8$ and $h_x/t = 0$, (c) $k_T a = 0$ and $h_x/t = 2.0$, and (d) $k_T a = \pi/8$ and $h_x/t = 2.0$. The vertical dashed lines located at $k_y a = \pm\pi/3$ indicate the boundaries of the magnetic Brillouin zone. The bulk bands have periodicity $2\pi/3a$, and the midgap edge bands have periodicity $2\pi/a$ along the k_y direction.

regions of overlap (because color degeneracies are only partially lifted by the color-flip field), as well as color-dependent midgap edge bands connecting bulk bands; and (d) $k_T a = \pi/8$ and $h_x/t = 2.0$, where there are nine sets of bulk bands connected by color-dependent midgap edge states, but residual bulk band overlaps are lifted by the additional presence of color-orbit coupling. All bulk bands have momentum space periodicity of $2\pi/3a$, while all edge bands have period $2\pi/a$ along the k_y direction. It is important to point out that there are potential experimental techniques to image edge states directly [44] in the context of ultracold atoms. The periodicity of the bulk states is determined by the denominator q of the rational magnetic flux ratio $\alpha = p/q$, which for $\alpha = 1/3$ corresponds to $q = 3$. In Fig. 1, the vertical dashed lines specify the boundaries of the magnetic Brillouin zone at $k_y a = \pm\pi/3$.

Now that we have obtained the eigenspectrum of the system and identified the existence of midgap edge states connecting different mixed-color bands, we discuss next the associated Chern numbers for the colored fermions.

IV. COLOR CHERN NUMBERS

The computation of the Chern numbers for color fermions can be performed in two different ways, either as bulk topological invariant for the toroidal geometry, or by analyzing the total chirality of edge states in the cylindrical geometry and relying on the bulk-edge correspondence [45] to extract the Chern numbers. In this section, we obtain the Chern numbers in both ways independently to guarantee that we obtain the correct results.

First, we calculate the Chern numbers as a bulk topological invariant. We impose periodic boundary conditions along the

x and y directions, and compactify the cylinder into a torus. To identify topologically nontrivial mixed-color bands and extract their Chern indices, we fix the flux ratio to the rational number $\alpha = p/q$, and write the color-dependent Harper's Hamiltonian as a $3q \times 3q$ matrix

$$\mathbf{H}(k_x, k_y) = \begin{pmatrix} \mathbf{H}_{RR} & \mathbf{H}_{RG} & \mathbf{H}_{RB} \\ \mathbf{H}_{GR} & \mathbf{H}_{GG} & \mathbf{H}_{GB} \\ \mathbf{H}_{BR} & \mathbf{H}_{BG} & \mathbf{H}_{BB} \end{pmatrix} \tag{7}$$

in momentum (k_x, k_y) space, by taking advantage of the magnetic translation group. We define $q \times q$ block matrices $\mathbf{H}_{cc'}$, where c and c' label the three color states $\{R, G, B\}$. The color-diagonal $q \times q$ block matrices $\mathbf{H}_{cc}$ are

$$\begin{pmatrix} \Gamma_1 & -te^{ik_{xc}a} & 0 & \dots & -te^{-ik_{xc}a} \\ -te^{-ik_{xc}a} & \Gamma_2 & -te^{ik_{xc}a} & \dots & 0 \\ \vdots & \vdots & \vdots & \ddots & \vdots \\ -te^{ik_{xc}a} & 0 & \dots & -te^{-ik_{xc}a} & \Gamma_q \end{pmatrix},$$

where $k_{xc} = k_x - \gamma_c k_T$ is the color-dependent momentum along the x direction, including the color-dependent momentum transfer $\gamma_c k_T$, with $\gamma_R = +1$, $\gamma_G = 0$, and $\gamma_B = -1$. The kinetic energy terms are $\Gamma_m = -2t\cos(k_y a - 2\pi\alpha m)$, where the magnetic flux ratio is $\alpha = p/q$ and m takes values $(1, ..., q)$. The color-off-diagonal $q \times q$ block matrices are $\mathbf{H}_{RB} = \mathbf{H}_{BR} = \mathbf{0}$ and $\mathbf{H}_{RG} = \mathbf{H}_{GR} = \mathbf{H}_{GB} = \mathbf{H}_{BG} = \mathbf{H}_{\text{flip}}$, where

$$\mathbf{H}_{\text{flip}} = \begin{pmatrix} -h_x/\sqrt{2} & 0 & 0 & 0 & 0 \\ 0 & -h_x/\sqrt{2} & 0 & 0 & 0 \\ \vdots & \vdots & \vdots & \ddots & \vdots \\ 0 & 0 & \dots & 0 & -h_x/\sqrt{2} \end{pmatrix} \tag{8}$$

describes color flips between R and G states, as well as between G and B states, via the color-flip field h_x.

Next, we analyze the Chern numbers for different values of color-orbit coupling and color-flip fields, but fixed flux ratio $\alpha = p/q$. The energy spectrum associated with the Hamiltonian $\mathbf{H}(k_x, k_y)$ in Eq. (7) has $3q$ color-magnetic bands $E_{\ell_\gamma}(\mathbf{k})$ that are labeled by a magnetic band number ℓ_γ with generalized color index γ corresponding to mixed color states, which we identify as cyan (C), magenta (M), and yellow (Y) or via a pseudospin basis $\{C, M, Y\} \to \{\Uparrow, 0, \Downarrow\}$. The minimum number of gaps between bulk bands is $q - 1$, when the bands are triply degenerate and the maximum is $3q - 1$, when there is no overlap between the bands.

The Chern index for the ℓ_γ^{th} band with generalized color index γ is

$$C_{\ell_\gamma} = \frac{1}{2\pi i}\int_{\partial\Omega} d^2\mathbf{k} F_{xy}^{(\ell_\gamma)}(\mathbf{k}), \tag{9}$$

where the domain of integration $\partial\Omega$ in momentum space corresponds to the magnetic Brillouin zone, that is, $\partial\Omega_x = [-\pi/a, \pi/a]$ along the k_x direction and $\partial\Omega_y = [-\pi/qa, \pi/qa]$ along the k_y direction. The function

$$F_{xy}^{(\ell_\gamma)}(\mathbf{k}) = \partial_x A_y^{(\ell_\gamma)}(\mathbf{k}) - \partial_y A_x^{(\ell_\gamma)}(\mathbf{k}) \tag{10}$$

is the Berry curvature expressed in terms of the Berry connection $A_j^{(\ell_\gamma)}(\mathbf{k}) = \langle u_{\ell_\gamma}(\mathbf{k})|\partial_j|u_{\ell_\gamma}(\mathbf{k})\rangle$, where $|u_{\ell_\gamma}(\mathbf{k})\rangle$ are the eigenstates of the Hamiltonian $\mathbf{H}(k_x, k_y)$ defined in Eq. (7). In the limit of zero color-orbit coupling ($k_T = 0$) and zero color-flip field ($h_x = 0$), the energy spectrum for flux ratio $\alpha = p/q$ has triply degenerate q magnetic bands and $q - 1$ gaps, such that the Chern index from Eq. (9) acquires a similar form to that found in the quantum Hall effect literature for spin-1/2 systems [46,47].

Chern indices are properties of bands $E_{\ell_\gamma}(\mathbf{k})$ or band bundles with degeneracy D and are computed using a discretized version of Eq. (9) via a generalization of the method used for spin-1/2 systems [48]. However, Chern numbers are defined within band gaps and depend on which gap the chemical potential is located. If the chemical potential μ is located in a band gap labeled by index r and corresponding to filling factor $\nu = r/q$, then the Chern number at this value of μ is

$$C_r = \sum_{\ell_\gamma, E<\mu}^{\nu=r/q} C_{\ell_\gamma}, \tag{11}$$

that is, the sum of Chern indices of bands with energies $E < \mu$, which characterize the insulating state labeled by the gap index r and filling factor $\nu = r/q$. Using our normalization, the maximum filling factor is $\nu_{\max} = 3$, indicating that the maximum number of color states per site is three.

We have also investigated the Chern numbers by analyzing the total chirality of the midgap edge states that arise in the cylindrical geometry. We found that they coincide with the Chern numbers C_r calculated from the toroidal geometry (bulk system without edges), as expected due to the bulk-edge correspondence [45]. The fact that these results agree for all insulating phases reassures us that the Chern numbers are calculated correctly.

From an analysis of the energy spectrum in Fig. 1 and the Chern numbers above, it is clear that the filling factor $\nu = r/q$ associated with the bulk gap r is a good label for the insulating phases in conjunction with Chern numbers C_r. Thus, we discuss next a gap labeling theorem that connects ν and C_r.

V. GAP LABELLING THEOREM

For spin-1/2 fermions in condensed matter systems, a gap labeling theorem that relates the filling factor $\nu = r/q$ and the magnetic flux parameter $\alpha = \Phi/\Phi_0 = p/q$ was found by Wannier and Claro [49,50]. In that case, the Zeeman field h_x was neglected and the theorem covered only couplings to the charge degrees of freedom of the system. However, in the present case, it is clear that the color-flip fields h_x play an important role in creating additional gaps, as we have seen in the discussion of Fig. 1. As h_x/t varies from $h_x/t \ll 1$ to $h_x/t \gg 1$, the number of gaps grows from two to eight.

We can establish a relation between the Chern numbers C_r, the magnetic ratio $\alpha = p/q$ and the filling factor $\nu = r/q$ by rewriting the Diophantine equation

$$r = qS_r + pC_r, \tag{12}$$

where the integer index r labels the gaps in the energy spectrum $E_{\ell_\gamma}(k_x, k_y)$ of the toroidal geometry, C_r is the Chern number for the rth gap, and S_r is a supplementary topological invariant. This equation can be expressed in terms of the filling

factor $\nu = r/q$ and the magnetic ratio $\alpha = p/q$ as

$$\nu = S_r + \alpha C_r. \tag{13}$$

The relation shown above generalizes the gap labeling theorem [49,50] used in the context of the integer quantum Hall effect, because the topological quantum numbers (S_r, C_r) change not only as a function of the magnetic ratio α but also as a function of the color-flip field h_x/t and color-orbit parameter $k_T a$, that is, $S_r(h_x/t, k_T a)$ and $C_r(h_x/t, k_T a)$. Notice that the maximal value of S_r for a given gap labeled by r is linked to the minimum value of C_r and vice versa, that is, $S_{r,\max} = \nu - \alpha C_{r,\min}$ and $S_{r,\min} = \nu - \alpha C_{r,\max}$.

For three color states, the integer values of r range from 0 to $3q$, when $\nu = 0$ and $\nu = 3$, respectively. We can use particle-hole symmetry (PHS) to relate the invariants S_r, C_r, and S_{3q-r}, C_{3q-r}. Applying PHS to the gap-labeling relation in Eq. (13) means making the transformation $\nu \to (3 - \nu)$ and $r \to (3q - r)$. For fixed α, h_x/t, and $k_T a$, due to total charge conservation, PHS requires that

$$C_{3q-r} = -C_r, \tag{14}$$

which then leads to the relation

$$S_{3q-r} = 3 - S_r. \tag{15}$$

These two relations can also be verified independently via the direct calculation of Chern numbers C_r and filling factors ν for fixed α, h_x/t, and $k_T a$.

The physical interpretation of the topological invariants C_r and S_r are as follows. The Chern number C_r was shown [46] to be directly related to the quantization of the Hall conductance

$$\tilde{\sigma}_{yx} = \frac{e^2}{h} C_r, \tag{16}$$

when the chemical potential μ lies in energy gap r. The physical interpretation of S_r reflects the quantization of the induced charge density

$$\tilde{\rho}_i = \frac{e}{a^2} S_r \tag{17}$$

due to screening originating from the lattice potential modulation.

The relation between $\tilde{\rho}_i$ and S_r is best understood as follows. Let us consider the action of the Lorentz force caused by the magnetic field $H\hat{\mathbf{z}}$ on a particle with band velocity v_y and the compensating effect of the induced electric field E_x in the cylindrical geometry with length L_x along the x direction and periodic boundary conditions along the y direction. When these forces are balanced, we have $ev_y H/c = eE_x$. We can express the Hall current density $\mathcal{J}_y$ as the flow of the transport charge density $\tilde{\rho}_t = \tilde{\rho} - \tilde{\rho}_i$, where $\tilde{\rho}$ is the charge density and $\tilde{\rho}_i$ is the induced charge density due to screening by the lattice potential, via

$$\mathcal{J}_y = \tilde{\rho}_t v_y. \tag{18}$$

Next, we use the Hall electric field E_x to write the Hall conductance as

$$\tilde{\sigma}_{yx} = \frac{\mathcal{J}_y}{E_x} = c\frac{\tilde{\rho}_t}{H}. \tag{19}$$

We define the transport charge density $\tilde{\rho}_t = en_t$ in terms of the transport particle density $n_t = N_t/L_x L_y$, where the product $L_x L_y$, with $L_x = N_x a$ and $L_y = N_y a$, is the area of the sample and N_t is the transport particle number. Substituting this definition into Eq. (19), we obtain the Hall conductance

$$\tilde{\sigma}_{yx} = c\frac{eN_t}{L_x L_y H} = \frac{N_t}{N_x N_y}\frac{ce}{\Phi}, \tag{20}$$

where the usual magnetic flux per lattice plaquette is $\Phi = Ha^2$. Notice that $N_t = N - N_i$, where N is the particle number and N_i is the induced particle number due to screening of the lattice potential. This means that $\nu_t = N_t/N_x N_y$ is nothing but the fraction of transported particles per site, that is, $\nu_t = \nu - \nu_i$, where ν is the filling factor and ν_i is the induced filling factor due to the lattice potential screening. Comparing the two relations in Eqs. (16) and (20), we can write $\nu_t = [\Phi/\Phi_0]C_r$, which immediately gives the relation

$$\nu = \nu_i + \alpha C_r, \tag{21}$$

where $\alpha = \Phi/\Phi_0$. This is the same expression written in Eq. (13), with the identification that the induced filling factor $\nu_i = S_r$. Since, $\nu_i = N_i/N_x N_y$, the induced charge density is

$$\tilde{\rho}_i = \frac{eN_i}{L_x L_y} = \frac{e}{a^2}\nu_i, \tag{22}$$

leading to the quantization of the induced charge density announced in Eq. (17).

We would like to note that when the lattice potential is zero, there is no induced charge $\tilde{\rho}_i$ and $S_r = 0$ in the continuum limit at every bulk gap. However, in the presence of lattice potentials, S_r can take nonzero integer values. Thus, to identify each insulating phase in optical lattices, we use not only the Chern number C_r, but also the filling factor ν or the supplementary topological invariant S_r, as discussed above. Having introduced the gap labeling relation that connects filling factors ν, magnetic flux ratio α, and topological numbers (S_r, C_r), we will use this ordered pair to classify the topological phases in the *charge* sector, noting that additional topological numbers may arise in the *color* sector, as discussed next.

VI. PHASE DIAGRAMS OF COLOR FERMIONS

Since we are interested in the effects of color-orbit coupling k_T and color-flip field h_x, we focus on phase diagrams for constant flux ratio $\alpha = p/q$, and choose the particular value of $\alpha = 1/3$, where nontrivial topological properties emerge. We use the Chern numbers defined in Eq. (11) and the gap labeling theorem of Eq. (13) to classify the topological phases in the phase diagrams of chemical potential μ versus color-flip field h_x and μ versus color-orbit coupling k_T. In some situations, we need to refine the topological classification to distinguish phases with the same *charge* Chern numbers and include an analysis of the *color* degrees of freedom together with the monitoring of the properties of midgap edge states.

A. Chemical potential versus color-flip field

In Fig. 2, we show phase diagrams of chemical potential μ/t versus the color-flip field h_x/t for fixed value of the magnetic flux ratio $\alpha = 1/3$ with four values of the color-orbit

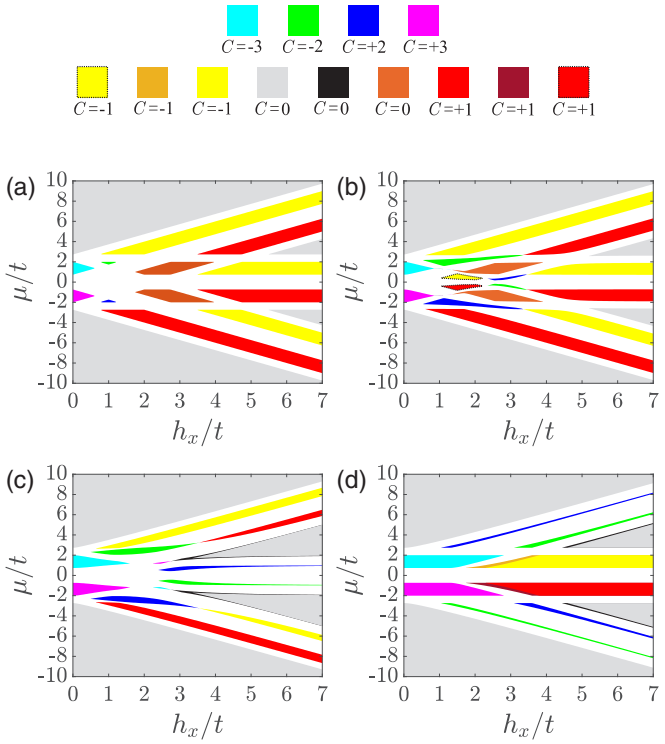

FIG. 2. Phase diagrams of chemical potential μ/t vs color-flip field h_x/t are shown for spin-orbit coupling parameters: (a) $k_T a = 0$, (b) $k_T a = \pi/8$, (c) $k_T a = \pi/2$, and (d) $k_T a = \pi$. The white regions correspond to gapless (*conducting*) phases, where the chemical potential lies within a band of states, while the nonwhite regions correspond to insulating phases. The Chern numbers of the insulating phases are shown in the color palette.

parameter: $k_T a = 0$, $k_T a = \pi/8$, $k_T a = \pi/2$, and $k_T a = \pi$. From the figures, it is clear that phase diagrams are quite complex, in particular for values of $h_x/t > 1$. But, before we embark on the description of the phase diagrams, we discuss first the labeling of the regions indicated in the legend of the figure.

In Fig. 2, the white regions correspond to gapless (*conducting*) phases, where the chemical potential lies within a band of states, while the nonwhite (colored) regions correspond to insulating phases, where the chemical potential lies within the gaps between bands of states. The legend in this figure is a color palette describing the Chern numbers for each colored region.

Given that certain regions with different colors have the same Chern numbers, it is clear that additional properties are needed to distinguish them. Before we discuss important aspects of the phase diagrams, we describe first the color palette. The magenta (cyan) regions with Chern number $+3$ (-3) possess three chiral midgap edge states with positive (negative) chirality, while the blue (green) regions with Chern number $+2$ (-2) possess two chiral midgap edge states with positive (negative) chirality. The red (yellow) regions with Chern number $+1$ (-1) possess one chiral midgap edge state with positive (negative) chirality; the dark red (dark yellow) regions with Chern number $+1$ (-1) possess not only one chiral midgap edge state with positive (negative) chirality, but also present achiral midgap edge states; nevertheless they are not topologically distinct from their parent red (yellow) regions. However, the regions that are red with black dots (yellow with black dots) with Chern number $+1$ (-1) have three chiral midgap edge states, two of which have positive (negative) chirality and one of which has negative (positive) chirality. Therefore, these insulating regions are topologically distinct from the red (yellow) regions with the same Chern numbers. The gray regions with Chern number 0 are topologically trivial with no chiral or achiral midgap edge states. The black regions with Chern number 0 are also topologically trivial with no chiral midgap edge states but with achiral midgap edge states. These black regions are not topologically distinct from the gray regions. Lastly, the orange regions with Chern number 0 are topologically nontrivial and possess two chiral midgap edge states with opposite chirality, reminiscent of the quantum spin Hall effect in spin-1/2 fermions.

There are a few general properties of the phase diagrams of Fig. 2 that we would like to highlight below. The first thing to notice is that Chern numbers for fixed h_x/t have odd symmetry upon reflection through $\mu = 0$. A change in *charge* from particle-like to hole-like leads to a flip in the chirality of the edge states, that is, a change in sign of the Chern number defined in Eq. (11). This property of the Chern number spectrum is a consequence of the particle-hole symmetry (PHS) of Hamiltonians Eqs. (1) or (5) about the line $\mu = 0$.

For fixed flux ratio $\alpha = 1/3$ and color-orbit parameter $k_T a$, the number of insulating phases, where gaps between energy bands exist, grows from two to eight with increasing color-flip parameter h_x/t from $h_x/t \ll 1$ to $h_x/t \gg 1$. This situation does not occur in electronic systems with spin-1/2 since the Zeeman field h_x cannot be tuned independently from the magnetic ratio α as they have the same origin, and typically h_x has very small values in comparison to the hopping parameter t, such that $h_x/t \ll 1$. However, for ultracold fermions, since h_x is a synthetic field that can be tuned independently from the magnetic ratio α, it can attain high values in comparison to t and provide access to phases that are not encountered in standard condensed matter systems.

In the regime $h_x/t \ll 1$, where the color splitting caused by the color-flip field h_x is small in comparison to the hopping t, we have essentially color unpolarized phases. In this case, the energy spectrum has only two gaps, similar to the cases illustrated in Figs. 1(a) and 1(b). Thus, only two insulating phases emerge: one with Chern number $+3$ (magenta) at the first gap and the other -3 (cyan) at the second gap. These phases are the color generalizations of the quantum Hall phases for spin-1/2 systems.

In the regime $h_x/t \gg 1$, where the color splitting caused by the color-flip field h_x is large in comparison to the hopping t, the system is essentially polarized in a mixed-color basis of the color (pseudospin) matrix $\mathbf{J}_x$ described in Eq. (5). In this case, the color-orbit parameter $k_T a$ lifts band degeneracies and creates eight gapped phases. In Figs. 2(a) and 2(b), where $k_T a \ll \pi$, the eight color-insulating phases have Chern numbers $+1$ (red), -1 (yellow), and 0 (gray), when $h_x/t \gg 1$. However, when color-orbit coupling $k_T a$ is sufficiently large, the mixed color bands get strongly coupled and the nature of the insulating phases changes dramatically. This can be seen in Fig. 2(c) for $k_T a = \pi/2$, where the insulating phases have

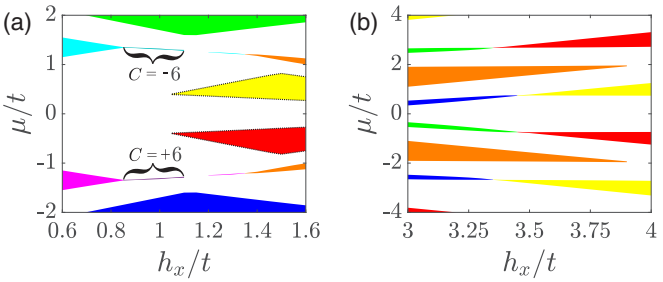

FIG. 3. Enlarged sections of the phase diagram shown in Fig. 2(b), where $k_T a = \pi/8$. The color code is the same used in the palette of Fig. 2.

Chern numbers $+1$ (red), -1 (yellow), 0 (gray), -2 (green), and $+2$ (blue) as well as in Fig. 2(d) for $k_T a = \pi$, where the insulating phases have Chern numbers -2 (green), $+2$ (blue), 0 (gray), $+1$ (red), and -1 (yellow).

In Fig. 3, we show enlarged sections of Fig. 2(b) to illustrate the most interesting aspects of the phase diagrams discussed so far. First, notice in Fig. 3(a) the very narrow regions with Chern numbers $+6$ at $\nu = 1$ and -6 at $\nu = 2$, reflecting the existence of six chiral edge states. These phases with high value of the Chern number exhibit the standard quantum Hall effect, which we name from now on as the quantum charge Hall (QChH) effect. There is nothing corresponding to the aforementioned phases for SU(2) fermions, since the latter systems possess a maximum of two chiral edge states throughout their phase diagrams. Second, notice in Figs. 3(a) and 3(b) the orange regions with zero Chern number at filling factors $\nu = 1$ and $\nu = 2$. This region has two chiral midgap edge states with opposite chiralities, producing a phase that we name quantum color Hall (QCoH) insulator, in analogy to the quantum spin Hall (QSH) insulator that exhibits the quantum spin Hall effect. These orange regions are the color versions of the QSH phases for spin-1/2 fermions [28–30]. Third, in Fig. 3(a), notice the region that is red with black dots (yellow with black dots) with Chern number $+1$ (-1) at $\nu = 4/3$ $(\nu = 5/3)$, which contains three midgap edge states, two with positive (negative) chirality and one with negative (positive) chirality, thus possessing the QChH effect. However, two of the midgap edge states with opposite chirality have different mixed-color indices leading also to a quantum color Hall (QCoH) effect. The simultaneity of QChH and QCoH in these phases is unique, since there is nothing corresponding to this for SU(2) fermions, that is, in spin-1/2 systems there are no phases that exhibit simultaneously the quantum Hall and the quantum spin Hall effect, unless they are fully spin polarized. These QCoH phases manifested in the analysis of midgap edge states suggest the need to establish bulk topological invariants (color-Hall Chern numbers) related to color-Hall conductances, whenever appropriate. Lastly, notice the existence of direct phase transitions between insulating states, namely the blue (green) and yellow (red) phases, occuring at $\nu = \{2/3, 5/3\}$ $(\nu = \{4/3, 7/3\})$, where the bulk gap closes only at one point in the phase diagram. This is also a special situation, as most phase transitions seen in Fig. 2 occur between an insulating (colored) and a *conducting* (white) phase.

$k_T a = \frac{\pi}{8}$ and $\frac{h_x}{t} = 2.0$

ν	Phase	S_r	C_r
1/3		0	+1
2/3		0	+2
1		+1	0
4/3		+1	+1
5/3		+2	-1
2		+2	0
7/3		+3	-2
8/3		+3	-1

$k_T a = \frac{\pi}{8}$ and $\frac{h_x}{t} = 3.0$

ν	Phase	S_r	C_r
1/3		0	+1
2/3		0	+2
1		+1	0
4/3		+2	-2
5/3		+1	+2
2		+2	0
7/3		+3	-2
8/3		+3	-1

FIG. 4. Tables illustrating the gap labeling theorem for two cuts in the phase diagram of Fig. 2(b). The table at left is for $k_T a = \pi/8$ and $h_x/t = 2.0$, while the table at right is for $k_T a = \pi/8$ and $h_x/t = 3.0$. The filling factor is $\nu = r/3$, where r is an integer from the set $\{1, 2, 3, 4, 5, 6, 7, 8\}$.

To illustrate the gap labeling theorem for the *charge* degrees of freedom, we show two tables in Fig. 4 corresponding to two cuts in Fig. 2(b), where $k_T a = \pi/8$ and $\alpha = 1/3$. The first cut is at $h_x/t = 2.0$ and the second is at $h_x/t = 3.0$. Both tables describe eight insulating phases located at band gaps labeled by $r = \{1, 2, 3, 4, 5, 6, 7, 8\}$. Each phase is labeled by the order pair (S_r, C_r) or (ν, C_r) as described in Sec. V. Theses tables also summarize some of the phases encountered in Fig. 2 and illustrate the symmetry relations $S_{9-r} = 3 - S_r$ and $C_{9-r} = -C_r$ under the particle-hole symmetry operation $\nu \to (3 - \nu)$ or $r \to (9 - r)$ when $q = 3$, as given in Eqs. (14) and (15).

B. Chemical potential versus color-orbit coupling

In Fig. 5, we show phase diagrams of chemical potential μ/t versus spin-orbit parameter $k_T a$ for fixed magnetic ratio $\alpha = 1/3$ and changing color-flip fields: (a) $h_x/t = 0$, (b) $h_x/t = 1.0$, (c) $h_x/t = 2.0$, and (d) $h_x/t = 3.0$. The color palette for insulating phases is the same used in Fig. 2. There are several general properties Fig. 5 that we would like to point out. We notice that the phase diagram of μ/t versus $k_T a$ has periodicity of 2π, inversion symmetry with respect to $k_T a = \pi$, and particle-hole symmetry with respect to $\mu = 0$. All these properties arise directly from symmetries of the Hamiltonian of the system discussed in Sec. II. Notice also that the lower and upper gray regions are topologically trivial and correspond to $\nu = 0$ with $(S_0, C_0) = (0, 0)$ and $\nu = 3$ with $(S_9, C_9) = (+3, 0)$, respectively. Furthermore, for fixed h_x/t, there are a few additional phases with high Chern number and several topological quantum phase transitions that occur between different insulating phases as $k_T a$ is changed. These phases are highlighted next.

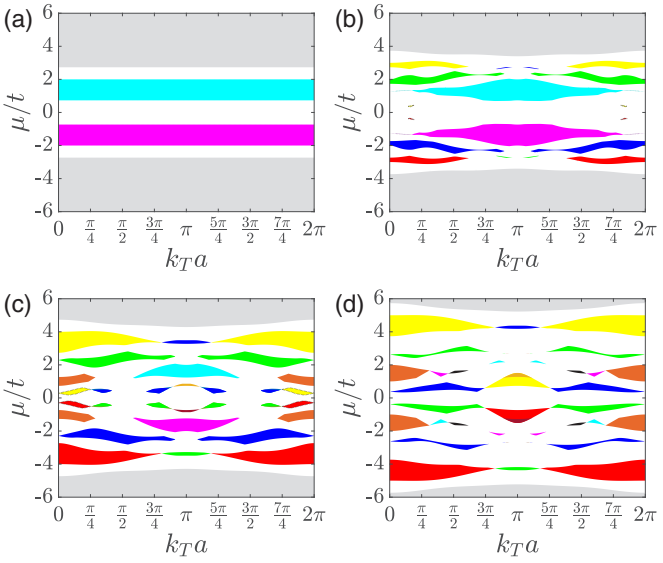

FIG. 5. Chemical potential μ/t vs spin-orbit parameter $k_T a$ for flux ratio $\alpha = 1/3$ and color-flip fields: (a) $h_x/t = 0$, (b) $h_x/t = 1.0$, (c) $h_x/t = 2.0$, and (d) $h_x/t = 3.0$. The color palette for insulating phases is the same used in Fig. 2.

In Fig. 6, we show enlarged sections of phase diagrams displayed in Figs. 5(b)–5(d). In Fig. 6(a), we show a region from Fig. 5(b), where $h_x/t = 1.0$. In Fig. 6(b), we display a region from Fig. 5(c), where $h_x/t = 2.0$. In Figs. 6(c) and 6(d), we illustrate regions of Fig. 5(d), where $h_x/t = 3.0$. The color code is the same as in Fig. 5. In Fig. 6(a), we highlight the high Chern number phases (± 6), which are hard to see in Fig. 5(b) and that have direct topological phase transitions to

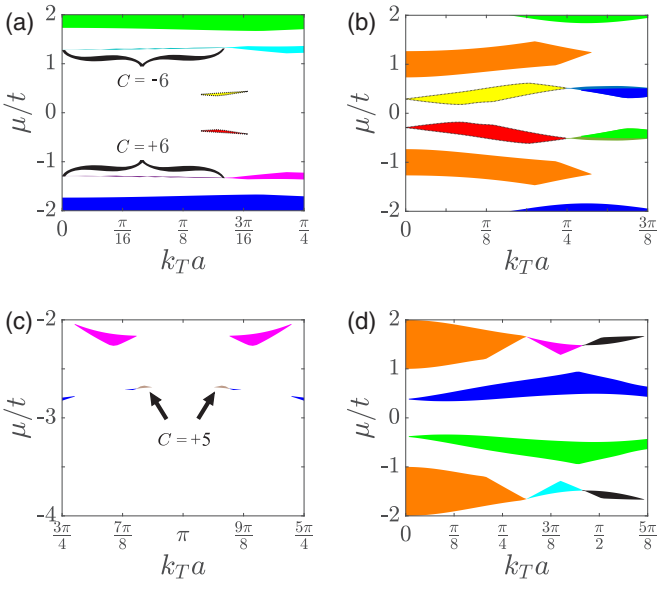

FIG. 6. Enlarged sections of phase diagrams shown in Figs. 5(b), 5(c) and 5(d). The section in panel (a) reflects a region of Fig. 5(b), where $h_x/t = 1.0$. The section in panel (b) reflects a region of Fig. 5(c), where $h_x/t = 2.0$. The sections in panels (c) and (d) show regions of Fig. 5(d), where $h_x/t = 3.0$. The color code is the same as in Fig. 2.

$k_T a = \frac{3\pi}{4}$ and $\frac{h_x}{t} = 2.0$

ν	Phase	S_r	C_r
1/3		0	+1
2/3		0	+2
1		0	+3
4/3		+2	-2
5/3		+1	+2
2		+3	-3
7/3		+3	-2
8/3		+3	-1

$k_T a = \pi$ and $\frac{h_x}{t} = 2.0$

ν	Phase	S_r	C_r
1/3		+1	-2
1		0	+3
4/3		+1	+1
5/3		+2	-1
2		+3	-3
8/3		+2	+2

FIG. 7. Tables illustrating the gap labeling theorem for two cuts in the phase diagram of Fig. 5(c). The table at left is for $k_T a = 3\pi/4$ and $h_x/t = 2.0$, while the table at right is for $k_T a = \pi$ and $h_x/t = 2.0$. The filling factor is $\nu = r/3$, where r is an integer from the set $\{1, 2, 3, 4, 5, 6, 7, 8\}$ that labels a band gap.

the magenta and cyan phases. In Fig. 6(b), we can see clearly direct topological phase transitions between the phases shown as red with black dots (yellow with black dots) and those shown as dark green (light blue) phases. The dark green (light blue) phases are not topologically distinct from the green (blue) phases, but in addition to two chiral edge states, they also possess achiral midgap states. In Fig. 6(c), we highlight the high Chern number ($+5$) phases, which are hard to see in Fig. 5(d) and that have direct topological phase transitions to blue phases. In Fig. 6(d), we can see clearly direct topological phase transitions between the orange and magenta (orange and cyan) as well as magenta and black (cyan and black) phases. The direct phase transitions between topological insulating phases occur only at one point in the phase diagrams, where the band gap closes at the transition point, but immediately reopens on either side of the transition with a new Chern number.

In Fig. 7, we show tables illustrating the gap labeling theorem for two cuts in the phase diagram of Fig. 5(c). The table at left is for $k_T a = 3\pi/4$ and $h_x/t = 2.0$, while the table at right is for $k_T a = \pi$ and $h_x/t = 2.0$. The table at left (right) describes eight (six) insulating phases corresponding to eight (six) gaps labeled by $r = \{1, 2, 3, 4, 5, 6, 7, 8\}$ ($r = \{1, 3, 4, 5, 6, 8\}$). The insulating phases are identified by the pairs (S_r, C_r) or (ν, C_r), where $\nu = r/3$. The symmetry relations $S_{9-r} = 3 - S_r$ and $C_{9-r} = -C_r$ under the particle-hole symmetry are again satisfied.

VII. COLOR DENSITY OF STATES

In conjunction with the energy spectrum $E_{n_\beta}(k_y)$ with open boundary conditions or $E_{\ell_\gamma}(k_x, k_y)$ with periodic boundary conditions for fixed magnetic flux $\alpha = p/q$, the total color

density of states $\rho(E)$ and the color density of states $\rho_c(E)$ for color c are useful quantities to identify the location of gapped phases as a function of color-flip fields h_x/t and color-orbit coupling $k_T a$.

The density of states can be obtained from Green's (resolvent) operator,

$$\hat{\mathbf{G}}(z) = \frac{1}{z\mathbf{1} - \hat{\mathbf{H}}}, \tag{23}$$

whose matrix elements in the original color basis $\{R, G, B\}$ can be written as

$$G_{cc'}(z) = \sum_{n_\beta k_y} \frac{u_{n_\beta c}(k_y) u^*_{n_\beta c'}(k_y)}{z - E_{n_\beta}(k_y)}, \tag{24}$$

where $u_{n_\beta c}(k_y)$ are the color components of the eigenvectors of the Hamiltonian operator $\hat{\mathbf{H}}$ with open boundary conditions and eigenvalues $E_{n_\beta}(k_y)$. The summations over k_y cover the magnetic Brillouin zone $[-\pi/qa, \pi/qa]$ for bulk states and the range $[-\pi/a, \pi/a]$ for midgap edge states, where a is the square lattice unit cell length, and include all mixed-color band indices n_β.

We can also use the appropriate spectral decomposition for the case with periodic boundary conditions to obtain

$$G_{cc'}(z) = \sum_{\ell_\gamma k_x k_y} \frac{u_{\ell_\gamma c}(k_x, k_y) u^*_{\ell_\gamma c'}(k_x, k_y)}{z - E_{\ell_\gamma}(k_x, k_y)}, \tag{25}$$

where $u_{\ell_\gamma c}(k_x, k_y)$ are the color components of the eigenvectors of the Hamiltonian operator $\hat{\mathbf{H}}$ with periodic boundary conditions and eigenvalues $E_{\ell_\gamma}(k_x, k_y)$. Here, ℓ_γ labels the magnetic subbands for $\alpha = p/q$. The momentum summations are over $[-\pi/a, \pi/a]$ for k_x and over $[-\pi/qa, \pi/qa]$ for k_y, that is, the summations over $\{\ell_\gamma, k_x, k_y\}$ cover the magnetic Brillouin zone and all the mixed color bands labeled by ℓ_γ.

Within the magnetic Brillouin zone, the density of states of color c at energy E is

$$\bar{\rho}_c(E) = -\frac{1}{\pi} \lim_{\delta \to 0} \mathrm{Im} G_{cc}(z = E + i\delta), \tag{26}$$

where δ is a small imaginary part. The color density of states per site is

$$\rho_c(E) = \frac{\bar{\rho}_c(E)}{q}, \tag{27}$$

since there are q unit cells in real space. The color density of states $\bar{\rho}_c(E)$ in the magnetic unit cell integrates to q states over all energies. The color density of states per site $\rho_c(E)$ always integrates to 1, because we have a maximum of one state for a given color c. Within the magnetic Brillouin zone, the number of states of a given color c at the chemical potential μ is

$$\mathcal{N}_c(\mu) = \int_{\mathrm{E_{min}}}^{\mu} dE \bar{\rho}_c(E), \tag{28}$$

where E_{min} is the minimum energy in the spectrum. The maximum value of $\mathcal{N}_c(\mu)$ is $\mathcal{N}_{c,\mathrm{max}} = q$, since there is maximum of one color state c per site, and q is the number of sites contained in the real space magnetic unit cell. The filling factor for color

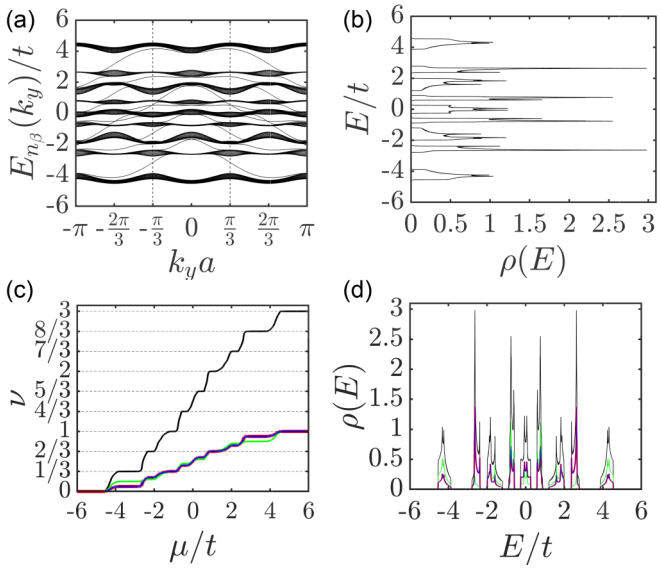

FIG. 8. Spectroscopic properties and filling factor for parameters $\alpha = 1/3$, $k_T a = \pi/8$, and $h_x/t = 1.85$. This corresponds to a vertical line across the phase diagram of Fig. 2(b). (a) Energy spectrum $E_{n_\beta}(k_y)/t$ vs $k_y a$ for the case of open boundary conditions, showing explicitly midgap edge states. The panels (b), (c), and (d) refer to the case of periodic boundary conditions. (b) Energy E/t vs total density of states per site $\rho(E)$ to illustrate that the gaps between bulk bands coincide with the gaps for the case of open boundary conditions. (c) Filling factor ν vs chemical potential μ/t showing steps where incompressible insulating phases occur. (d) Density of states per site $\rho(E)$ vs energy E/t. The total color density states per site $\rho(E)$ is in black, and the color density of states are in red for the red states, in green for the green states, and in blue for the blue states.

c is defined as the ratio

$$\nu_c(\mu) = \frac{\mathcal{N}_c(\mu)}{\mathcal{N}_{c,\mathrm{max}}}, \tag{29}$$

which has a maximal value of one, that is, $\nu_{c,\mathrm{max}} = 1$.

The total density of states within the magnetic unit cell can be written as

$$\bar{\rho}(E) = \sum_c \bar{\rho}_c(E), \tag{30}$$

while the total density of states per site has the form

$$\rho(E) = \frac{\bar{\rho}(E)}{q}. \tag{31}$$

The total density of states $\bar{\rho}(E)$, within the unit cell, integrates to $3q$ states over all energies, while the density of states per site $\rho(E)$ always integrates to 3, because we have a maximum of three colors per site. The total filling factor at chemical potential μ is

$$\nu(\mu) = \sum_c \nu_c(\mu), \tag{32}$$

having a maximum value $\nu_{\mathrm{max}} = 3$.

In Fig. 8, we show spectroscopic information for particular values of parameters: the magnetic flux ratio $\alpha = 1/3$, the color-flip field $h_x/t = 1.85$, and the color-orbit coupling parameter $k_T a = \pi/8$. All these parameters are the same for

Figs. 8(a) through 8(d). The choice of these parameters illustrates a vertical scan at $h_x/t = 1.85$ in Fig. 2(b). The vertical line cuts through a wide variety of topological phases as the chemical potential μ grows.

In Fig. 8(a), we show the energy eigenspectrum versus momentum $k_y a$ for open boundary conditions, where eight gaps can be seen in the spectrum corresponding to the insulating phases of the vertical scan in Fig. 2(b) at $h_x/t = 1.85$. The energy dispersions of the midgap edge states are also shown. The gaps are labeled by the index $r = \{1, 2, 3, 4, 5, 6, 7, 8\}$ and the insulating phases are exactly the same shown in Fig. 4 for the table at left.

In Fig. 8(b), we show a plot of energy E versus total color density of states per site $\rho(E)$ for periodic boundary conditions to indicate explicitly the location of the bulk gaps in the energy spectrum. We use a small imaginary part ($\delta = 5 \times 10^{-3} t$) to calculate $\rho(E)$ from $G_{cc}(z = E + i\delta)$. The eight energy gaps can be clearly seen at the locations where the total color density of states in the bulk is zero. The regions associated with these gaps correspond to the eight phases that are crossed in a vertical scan in Fig. 2(b) at $h_x/t = 1.85$ as the chemical potential μ or filling factor ν grows. The sequence of phases is the same as in the table at left for Fig. 4.

In Fig. 8(c), we show a plot of the color filling factors ν_c and the total filling factor ν versus chemical potential μ, calculated using the color density of states per site $\rho_c(E)$ and the total color density of states per site $\rho(E)$, respectively. Notice that when the chemical potential μ lies inside a band gap, the filling factor ν is constant and take the exact form $\nu = r/q$ as discussed in connection to the gap labeling theorem of Sec. V. When μ lies inside of a gap, the insulating phase is incompressible because the filling factors ν and ν_c are constant, that is, the color compressibility $\kappa_c = d\nu_c(\mu)/d\mu$ is equal to zero. Naturally, the sequence of insulating phases crossed as μ increases is exactly the same as that in Fig. 2(b), and the sequence of phases is the same as shown in the table at left of Fig. 4. Notice also that filling factors $\nu_R = \nu_B$ reflect a symmetry of the Hamiltonian operator in Eq. (1) via the simultaneous exchange $R \leftrightarrow B$ and $k_T \leftrightarrow -k_T$.

In Fig. 8(d), we show a plot of the color density of states per site ρ_c and the total color density of states per site ρ versus energy E. Notice that $\rho_R(E) = \rho_B(E)$, reflecting a symmetry of the Hamiltonian operator in Eq. (1) via the simultaneous exchange $R \leftrightarrow B$ and $k_T \leftrightarrow -k_T$. One can clearly see the eight bands characterizing the insulating states discussed in Fig. 8(c). The total color density states per site $\rho(E)$ is in black, and the color density of states are in red for the red states, in green for the green states, and in blue for the blue states.

VIII. EFFECTS OF INTERACTIONS

As discussed in the introduction, the fermionic atoms ^{87}Sr and ^{173}Yb have SU(N)-symmetric interactions. For ^{87}Sr, the atom-atom interactions are up to SU(10) symmetric, while for ^{173}Yb, the interactions are up to SU(6) symmetric. In this discussion, we consider only SU(3)-symmetric interactions, since it is experimentally possible to trap selectively any three states from the SU(6) or SU(10) manifold. The SU(3)-symmetric interactions between these closed-shell fermionic atoms are local in space and given by the contact term

$$\hat{H}_{\rm int} = U \sum_{\mathbf{r}} \sum_{c \neq c'} \hat{n}_c(\mathbf{r}) \hat{n}_{c'}(\mathbf{r}), \tag{33}$$

in the pure density-density channels. Notice that there are no color-exchange interactions. Here, $U > 0$, that is, the interactions are purely repulsive, and the density operators are simply $\hat{n}_c(\mathbf{r}) = \psi_c^\dagger(\mathbf{r})\psi_c(\mathbf{r})$. The position $\mathbf{r}$ is the ordered pair (x, y) indicating the position of the atoms in the two-dimensional lattice considered, and the operator $\psi_c^\dagger(\mathbf{r})$ creates a fermion of color c at position $\mathbf{r}$.

If the interactions are weak in comparison to insulating gaps, there is no dramatic effect on the insulating nature of the bulk states; however, the midgap edge states may be sensitive to weak interactions. So, to test the robustness of edge states with respect to interactions, we will consider next the limit where the onsite interaction U is much smaller than the hopping parameter t, that is, $U/t \ll 1$. The regime of $U/t \ll 1$ is easily attainable experimentally in optical lattices for small or moderate lattice depths [51], and it is sufficient for the present purposes. However, we mention in passing that one can reach also the limit of $U/t \gg 1$ for deeper lattices or by using orbital-Feshbach techniques to control the strength of the SU(N)-symmetric interactions [11,12].

To study the robustness of edge states to SU(3)-symmetric interactions existent in ^{173}Yb and ^{87}Sr, it is more convenient to write Eq. (33) in terms of the creation and annihilation operators of the eigenstates of the Hamiltonian matrix operator $\hat{\mathbf{H}}(\hat{\mathbf{k}})$ described in Eq. (5). We consider periodic boundary conditions only along the y direction; that is, we use the cylindrical geometry that produces the spectrum in Fig. 1, where edge states emerge. We note that the analysis performed below is equally applicable to the SU(N)-symmetric interactions, when more than three internal states are involved.

Since the interactions are local, only midgap edge states residing on the same edge interact with each other. Thus, in the basis of eigenstates of $\hat{\mathbf{H}}(\hat{\mathbf{k}})$ defined in Eq. (5), the SU(3)-symmetric interactions become

$$\hat{H}_{\rm int} = U \sum_{\{\chi_i\}} \Gamma_{\{\chi_i\}} f_{\chi_1}^\dagger f_{\chi_2} f_{\chi_3}^\dagger f_{\chi_4}, \tag{34}$$

where $\{\chi_i\} = \{\chi_1, \chi_2, \chi_3, \chi_4\}$. The operator $f_\chi^\dagger$ creates a fermion in the edge state $|\chi\rangle = |\lambda, k_y, n\rangle$, where $\lambda = \{R, L\}$ labels the boundary, k_y labels the momentum along the y direction, and n is the edge state band index. In addition, the tensor

$$\Gamma_{\{\chi_i\}} = \sum_i \sum_{c \neq c'} \phi_{\chi_1}^*(i, c)\phi_{\chi_2}(i, c)\phi_{\chi_3}^*(i, c')\phi_{\chi_4}(i, c') \tag{35}$$

is expressed in terms of eigenstate projections $\phi_\chi(i, c) = \langle i, c|\chi\rangle$, where we wrote the color index c explicitly to make it evident in the summations over colors.

Since momentum is conserved along the y direction, it is clear that the tensor $\Gamma_{\{\chi_i\}}$ is proportional to $\delta_{k_{y_1}+k_{y_3}, k_{y_2}+k_{y_4}}$. Furthermore, given that the interactions are local, the only nonvanishing contribution comes from $\lambda_1 = \lambda_2 = \lambda_3 = \lambda_4 = \lambda$, that is, when the interacting states are on the same edge. Therefore, we may write

$$\Gamma_{\{\chi_i\}} = \gamma(\lambda, \{n_i\})\delta_{k_{y_1}+k_{y_3}, k_{y_2}+k_{y_4}}, \tag{36}$$

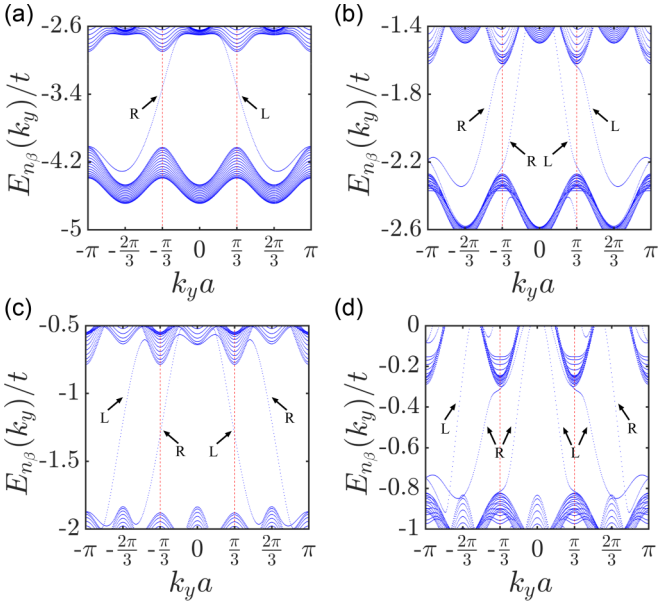

FIG. 9. Enlargements of energy dispersions vs momentum k_y to illustrate edge bands and their locations on the right (R) or left (L) boundaries along the x direction. All panels refer to phases shown in Fig. 2(b), where $k_T a = \pi/8$. In panel (a), we show the edge bands of the red phase edge for $h_x/t = 2.0$. In panel (b), we show edge bands of the blue phase for $h_x/t = 1.2$. In panel (c), we show the edge bands of the orange phase for $h_x/t = 2.5$. In panel (d), we show the edge bands of the phase marked in red with black dots for $h_x/t = 1.5$

where $\{n_i\} = \{n_1, n_2, n_3, n_4\}$ and the coupling between edge states on the same boundary is

$$\gamma(\lambda, \{n_i\}) = \sum_x \sum_{c \neq c'} R_{\lambda,n_1,n_2}(x,c) R_{\lambda,n_3,n_4}(x,c'), \tag{37}$$

with $R_{\lambda,n,n'}(x,c) = \phi^*_{\lambda,n}(x,c)\phi_{\lambda,n'}(x,c)$. Finally, we can write the SU(3)-symmetric interaction Hamiltonian for the edge states as

$$\hat{H}_{\rm int} = U \sum_{\lambda,\{n_i\}} \sum_{k_{y_1},k_{y_3},q_y} \gamma(\lambda,\{n_i\}) f^\dagger_{\lambda,n_1}(k_{y_1}) \times f_{\lambda,n_2}(k_{y_1}+q_y) f^\dagger_{\lambda,n_3}(k_{y_3}) f_{\lambda,n_4}(k_{y_3}-q_y). \tag{38}$$

From the expression above, it is clear that backscattering between two edge states on the same boundary is possible, and its strength depends on the precise values of the interaction parameters $\gamma(\lambda, \{n_i\})$. From the theory of interacting one-dimensional fermions [52], backscattering can produce density wave (DW) instabilities facilitated by momentum space nesting. This means that minigaps may arise in the excitation spectrum of edge states and color density waves (CoDW) may emerge at the boundaries.

In Fig. 9, we show edge bands for four enlarged regions of the phase diagram found in Fig. 2(b). Boundaries exist only along the x direction, so we label R and L as the right and left boundaries respectively, where edge states are located. The red phase with one chiral edge state and Chern number $+1$ is shown in Fig. 9(a). The blue phase with two chiral edge states and Chern number $+2$ is shown Fig. 9(b). The orange phase with two chiral edge states and Chern number 0 is shown in Fig. 9(c). The red-with-black-dots phase with three chiral edge states (two with chirality $+1$ and one with chirality -1) and Chern number $+1$ is shown in Fig. 9(d).

The only edge state in the red phase cannot exhibit backscattering, so there are no minigaps induced by weak SU(3) interactions, and the edge state is fully protected. The two edge states in the blue phase are also protected against backscattering as they have velocities with the same sign in a given boundary, so the local SU(3) interactions cannot open up minigaps and change the topological nature of these phases by inducing a color density wave. Thus, for weak local SU(3) interactions, the red and blue phases continue to exhibit quantized charge Hall conductances and their Chern numbers remain unchanged. By contrast, the edge states in the orange phase can exhibit backscattering since the states on the same boundary have opposite velocities. Therefore, minigaps can develop and a CoDW can emerge but the Chern number is unaffected, that is, it remains zero. However, the color-Hall conductance may not be quantized but would still have a nonzero value. The red-with-black dots phase is also sensitive to backscattering. The two outermost states with higher positive or lower negative momenta can backscatter each other and lead to minigaps, thus affecting the strict quantization of the color-Hall conductance but still producing a nonzero value. However, the innermost states with small positive or negative momenta are protected from backscattering, and as a result the phase shown by red with black dots continues to exhibit quantized charge Hall conductance and preserves its Chern number. In contrast, the color Hall conductance may not be quantized but still has a nonzero value.

Before concluding, we would like to point out that the regime of strong interactions ($U/t \gg 1$) in the presence of artificial gauge, color-orbit, and color-flip fields is also very interesting, since it may lead to novel physics beyond the traditional fractional quantum Hall effects and fractionally charged quasiparticles [53] encountered in SU(2) systems without considering spin degrees of freedom and their couplings to orbital motion. However, the regime of $U/t \gg 1$ is beyond the scope of this paper.

IX. SUMMARY AND CONCLUSIONS

We investigated the eigenspectrum, Chern numbers, and phase diagrams of ultracold color-orbit-coupled SU(3) fermions in optical lattices, having in mind possible experimental systems, such as fermionic isotopes ^{137}Yb and ^{87}Sr. We labeled the internal states of the atoms by colors red (R), green (G), and blue (B), and analyzed the quantum phases as a function of artificial magnetic, color-orbit, and color-flip fields that can be independently controlled.

For fixed artificial magnetic flux ratio, we identified topological quantum phases and phase transitions in the phase diagrams of chemical potential versus color-flip fields or color-orbit coupling, where the chirality and number of midgap edge states change. We established a gap labeling theorem to characterize the insulating phases by their filling factors and topological quantum numbers.

The topologically nontrivial phases were classified in three groups: The first group has total nonzero chirality and exhibits only the quantum charge Hall effect; the second

group has total nonzero chirality and exhibits both quantum charge and quantum color Hall effects; and the third group has total zero chirality but exhibits the quantum color Hall effect. These phases are generalizations of the quantum Hall and quantum spin Hall phases for charged spin-1/2 fermions.

We described the color density of states per site and a staircase structure in the total and color filling factors versus chemical potential for fixed color-orbit coupling, color-flip field, and magnetic flux ratio. We showed the existence of incompressible states at rational filling factors precisely given by a gap labeling theorem, which related the filling factors to the magnetic flux ratio and topological quantum numbers.

Lastly, we also analyzed the robustness of the topological insulating phases and their edge states with respect to weak SU(3) interactions and found that their topological properties remain largely intact in most cases.

Our theoretical findings pave the way for the experimental discovery of topological insulating phases that present simultaneously a quantum charge Hall effect (QChH) and a quantum color Hall effect (QCoH) in SU(3) fermions such as ^{173}Yb or ^{87}Sr. This particular phase has no correspondence for spin-1/2 fermions in condensed matter or ultracold atomic physics, where the quantum Hall and the quantum spin Hall phases are mutually exclusive. Furthermore, our work suggests the exploration of the effects of strong SU(3) interactions in the presence of artificial gauge, color-orbit, and color-flip fields, which may lead to novel physics beyond the fractional quantum Hall effect and fractionally charged quasiparticles encountered in SU(2) systems.

ACKNOWLEDGMENTS

One of us (C.A.R.S.d.M.) would like to thank the Galileo Galilei Institute for Theoretical Physics (Florence, Italy) for support via a Simons Fellowship and the International Institute of Physics (Natal, Brazil) for support via its Visitor's Program.

[1] T. Fukuhara, Y. Takasu, M. Kumakura, and Y. Takahashi, Degenerate Fermi Gases of Ytterbium, Phys. Rev. Lett. **98**, 030401 (2007).

[2] M. A. Cazalilla, A. F. Ho and M. Ueda, Ultracold gases of ytterbium: Ferromagnetism and Mott states in an SU(6) Fermi system, New. J. Phys. **11**, 103033 (2009).

[3] S. Taie, Y. Takasu, S. Sugawa, R. Yamazaki, T. Tsujimoto, R. Murakami, and Y. Takahashi, Realization of a SU(2) × SU(6) System of Fermions in a Cold Atomic Gas, Phys. Rev. Lett. **105**, 190401 (2010).

[4] S. Taie, R. Yamazaki, S. Sugawa, and Y. Takahashi, An SU(6) Mott insulator of an atomic Fermi gas realized by large-spin Pomeranchuk cooling, Nat. Phys. **8**, 825 (2012).

[5] G. Pagano, M. Mancini, G. Cappellini, P. Lombardi, Florian Schäfer, H. Hu, X.-J. Liu, J. Catani, C. Sias, M. Inguscio, and L. Fallani, A one-dimensional liquid of fermions with tunable spin, Nat. Phys. **10**, 198 (2014).

[6] C. Hofrichter, L. Riegger, F. Scazza, M. Höfer, D. R. Fernandes, I. Bloch, and S. Fölling, Direct Probing of the Mott Crossover in the SU(N) Fermi-Hubbard Model, Phys. Rev. X **6**, 021030 (2016).

[7] B. J. DeSalvo, M. Yan, P. G. Mickelson, Y. N. Martinez de Escobar, and T. C. Killian, Degenerate Fermi Gas of ^{87}Sr, Phys. Rev. Lett. **105**, 030402 (2010).

[8] M. K. Tey, S. Stellmer, R. Grimm, and F. Schreck, Double-degenerate Bose-Fermi mixture of strontium, Phys. Rev. A **82**, 011608(R) (2010).

[9] S. Stellmer, R. Grimm, and F. Schreck, Detection and manipulation of nuclear spin states in fermionic strontium, Phys. Rev. A **84**, 043611 (2011).

[10] S. Stellmer, F. Schreck, and T. C. Killian, Degenerate quantum gases of strontium, in *Annual Review of Cold Atoms and Molecules* (World Scientific, Singapore, 2014), Chap. 1, pp. 1–80.

[11] G. Pagano, M. Mancini, G. Cappellini, L. Livi, C. Sias, J. Catani, M. Inguscio, and L. Fallani, Strongly Interacting Gas of Two-Electron Fermions at an Orbital Feshbach Resonance, Phys. Rev. Lett. **115**, 265301 (2015).

[12] M. Höfer, L. Riegger, F. Scazza, C. Hofrichter, D. R. Fernandes, M. M. Parish, J. Levinsen, I. Bloch, and S. Fölling, Observation of an Orbital Interaction-Induced Feshbach Resonance in ^{173}Yb, Phys. Rev. Lett. **115**, 265302 (2015).

[13] N. Goldman, G. Juzeliūnas, P. Öhberg, and I. B. Spielman, Light-induced gauge fields for ultracold atoms, Rep. Prog. Phys. **77**, 126401 (2014).

[14] V. Galitski, G. Juzeliūnas, and I. B. Spielman, Artificial gauge fields with ultracold atoms, Phys. Today **72**, 38 (2019).

[15] Y.-J. Lin, R. L. Compton, K. Jiménez-García, J. V. Porto, and I. B. Spielman, Synthetic magnetic fields for ultracold neutral atoms, Nature (London) **462**, 628 (2009).

[16] M. Aidelsburger, M. Atala, M. Lohse, J. T. Barreiro, B. Paredes, and I. Bloch, Realization of the Hofstadter Hamiltonian with Ultracold Atoms in Optical Lattices, Phys. Rev. Lett **111**, 185301 (2013).

[17] H. Miyake, G. A. Siviloglou, C. J. Kennedy, W. C. Burton, and W. Ketterle, Realizing the Harper Hamiltonian with Laser-Assisted Tunneling in Optical Lattices, Phys. Rev. Lett. **111**, 185302 (2013).

[18] K. von Klitzing, G. Dorda, and M. Pepper, New Method for High-Accuracy Determination of the Fine-Structure Constant Based on Quantized Hall Resistance, Phys. Rev. Lett. **45**, 494 (1980).

[19] D. C. Tsui, H. L. Stormer, and A. C. Gossard, Two-Dimensional Magnetotransport in the Extreme Quantum Limit, Phys. Rev. Lett. **48**, 1559 (1982).

[20] P. G. Harper, Single band motion of conduction electrons in a uniform magnetic field, Proc. Phys. Soc. London A **68**, 874 (1955).

[21] D. R. Hofstadter, Energy levels and wave functions of Bloch electrons in rational, and irrational magnetic fields, Phys. Rev. B **14**, 2239 (1976).

[22] M. Aidelsburger, M. Lohse, C. Schweizer, M. Atala, J. T. Barreiro, S. Nascimbène, N. R. Cooper, I. Bloch, and N. Goldman, Measuring the Chern number of Hofstadter bands with ultracold bosonic atoms, Nat. Phys. **11**, 162 (2015).

[23] N. Dupuis, G. Montambaux, and C. A. R. Sá de Melo, Quasi-One-Dimensional Superconductors in Strong Magnetic Fields, Phys. Rev. Lett. **70**, 2613 (1993).

[24] G. Montambaux, N. Dupuis, and C. A. R. Sá de Melo, Quasi-one-dimensional superconductors in strong magnetic field, Phys. B (Amsterdam, Neth.) **194**, 1383 (1994).

[25] C. A. R. Sá de Melo, Paramagnetism and reentrant behavior in quasi-one-dimensional superconductors at high magnetic fields, Phys. C (Amsterdam, Neth.) **260**, 224 (1996).

[26] C. A. R. Sá de Melo, Singlet versus triplet superconductivity in quasi-one-dimensional systems: Magnetic field effects, in *The Superconducting State in Magnetic Fields: Special Topics and New Trends* (World Scientific, Singapore, 1998), pp. 296–324.

[27] Y.-J. Lin, K. Jiménez-García, and I. B. Spielman, Spin-orbit coupled Bose-Einstein condensates, Nature (London) **471**, 83 (2011).

[28] C. L. Kane and E. J. Mele, Z_2 Topological order and the Quantum Spin Hall Effect, Phys. Rev. Lett. **95**, 146802 (2005).

[29] L. Sheng, D. N. Sheng, C. S. Ting, and F. D. M. Haldane, Nondissipative Spin Hall Effect Via Quantized Edge Transport, Phys. Rev. Lett. **95**, 136602 (2005).

[30] B. A. Bernevig and S.-C. Zhang, Quantum Spin Hall Effect, Phys. Rev. Lett. **96**, 106802 (2006).

[31] N. Fläschner, B. S. Rem, M. Tarnowski, D. Vogel, D.-S. Lühmann, K. Sengstock, and C. Weitenberg, Experimental reconstruction of the Berry curvature in a Floquet Bloch band, Science **352**, 1091 (2016).

[32] E. Zhao, N. Bray-Ali, C. J. Williams, I. B. Spielman, and I. I. Satija, Chern numbers hiding in time-of-flight images, Phys. Rev. A **84**, 063629 (2011).

[33] P. Hauke, M. Lewenstein, and A. Eckardt, Tomography of Band Insulators from Quench Dynamics, Phys. Rev. Lett. **113**, 045303 (2014).

[34] G. Jotzu, M. Messer, R. Desbuquois, M. Lebrat, T. Uehlinger, D. Greif, and T. Esslinger, Experimental realization of the topological haldane model with ultracold fermions, Nature (London) **515**, 237 (2014).

[35] H. M. Price and N. R. Cooper, Mapping the Berry curvature from semiclassical dynamics in optical lattices, Phys. Rev. A **85**, 033620 (2012).

[36] A. Dauphin and N. Goldman, Extracting the Chern Number from the Dynamics of a Fermi Gas: Implementing a Quantum Hall Bar for Cold Atoms, Phys. Rev. Lett. **111**, 135302 (2013).

[37] W. Beugeling, N. Goldman, and C. Morais Smith, Topological phases in a two-dimensional lattice: Magnetic field versus spin-orbit coupling, Phys. Rev. B **86**, 075118 (2012).

[38] M. H. Yau and C. A. R. Sá de Melo, Chern-number spectrum of ultracold fermions in optical lattices tuned independently via artificial magnetic, Zeeman, and spin-orbit fields, Phys. Rev. A **99**, 043625 (2019).

[39] N. Goldman, I. Satija, P. Nikolic, A. Bermudez, M. A. Martin-Delgado, M. Lewenstein, and I. B. Spielman, Realistic Time-Reversal Invariant Topological Insulators with Neutral Atoms, Phys. Rev. Lett. **105**, 255302 (2010).

[40] D. Lao, C. Raman, and C. A. R. Sá de Melo, Nematic-Orbit Coupling and Nematic Density Waves in Spin-1 Condensates, Phys. Rev. Lett. **124**, 173203 (2020).

[41] D. M. Kurkcuoglu and C. A. R. Sá de Melo, Creating spin-one fermions in the presence of artificial spin-orbit fields: Emergent spinor physics and spectroscopic properties, J. Low Temp. Phys. **191**, 174 (2018).

[42] D. M. Kurkcuoglu and C. A. R. Sá de Melo, Color superfluidity of neutral ultracold fermions in the presence of color-flip and color-orbit fields, Phys. Rev. A **97**, 023632 (2018).

[43] R. Peierls, On the theory of diamagnetism of conduction electrons, Z. Phys. **80**, 763 (1933).

[44] N. Goldman, J. Dalibard, A. Dauphin, F. Gerbier, M. Lewenstein, P. Zoller, I. B. Spielman, Direct imaging of topological edge states in cold-atom systems, Proc. Natl. Acad. Sci. USA **110**, 6736 (2013).

[45] Y. Hatsugai, Topological aspects of the quantum Hall effect, J. Phys.: Condens. Matter **9**, 2507 (1997).

[46] D. J. Thouless, M. Kohmoto, M. P. Nightingale, and M. den Nijs, Quantized Hall Conductance in a Two-Dimensional Periodic Potential, Phys. Rev. Lett. **49**, 405 (1982).

[47] M. Kohmoto, Topological invariant and the quantization of the Hall conductance, Ann. Phys. **160**, 343 (1985).

[48] T. Fukui, Y. Hatsugai, and H. Suzuki, Chern numbers in discretized Brillouin zone: Efficient method of computing (spin) Hall conductances, J. Phys. Soc. Jpn. **74**, 1674 (2005).

[49] G. H. Wannier, A result not dependent on rationality for Bloch electrons in a magnetic field, Phys. Status Solidi B **88**, 757 (1978).

[50] F. H. Claro and G. H. Wannier, Magnetic subband structure of electrons in hexagonal lattices, Phys. Rev. B **19**, 6068 (1979).

[51] M. Greiner, O. Mandel, T. Esslinger, T. W. Hänsch, and I. Bloch, Quantum phase transition from a superfluid to a Mott insulator in a gas of ultracold atoms, Nature (London) **415**, 39 (2002).

[52] J. Solyom, The Fermi gas model of one-dimensional conductors, Adv. Phys. **28**, 201 (1979).

[53] R. B. Laughlin, Anomalous Quantum Hall Effect: An Incompressible Quantum Fluid with Fractionally Charged Excitations, Phys. Rev. Lett. **50**, 1395 (1983).